

Dark current mechanism of terahertz quantum-well photodetectors

J. Y. Jia, J. H. Gao, M. R. Hao, T. M. Wang, W. Z. Shen, Y. H. Zhang, J. C. Cao, X. G. Guo, and H. Schneider

Citation: *Journal of Applied Physics* **116**, 154501 (2014); doi: 10.1063/1.4898036

View online: <http://dx.doi.org/10.1063/1.4898036>

View Table of Contents: <http://scitation.aip.org/content/aip/journal/jap/116/15?ver=pdfcov>

Published by the [AIP Publishing](#)

Articles you may be interested in

[Terahertz quantum-well photodetectors: Design, performance, and improvements](#)

J. Appl. Phys. **114**, 194507 (2013); 10.1063/1.4826625

[Negative differential resistance induced by thermalization of two-dimensional electrons in terahertz quantum-well photodetectors](#)

J. Appl. Phys. **113**, 203109 (2013); 10.1063/1.4808343

[Background-limited terahertz quantum-well photodetector](#)

Appl. Phys. Lett. **86**, 231103 (2005); 10.1063/1.1947377

[Asymmetry in the dark current low frequency noise characteristics of B–B and B–C quantum well infrared photodetectors from 10 to 80 K](#)

J. Appl. Phys. **87**, 2400 (2000); 10.1063/1.372192

[Noise characteristics of quantum-well infrared photodetectors at low temperatures](#)

Appl. Phys. Lett. **76**, 206 (2000); 10.1063/1.125703



Dark current mechanism of terahertz quantum-well photodetectors

J. Y. Jia,¹ J. H. Gao,¹ M. R. Hao,¹ T. M. Wang,¹ W. Z. Shen,¹ Y. H. Zhang,^{1,a)} J. C. Cao,² X. G. Guo,² and H. Schneider^{3,b)}

¹Key Laboratory of Artificial Structures and Quantum Control (Ministry of Education), Department of Physics and Astronomy, Shanghai Jiao Tong University, Shanghai 200240, China

²Key Laboratory of Terahertz Solid-State Technology, Shanghai Institute of Microsystem and Information Technology, Chinese Academy of Sciences, 865 Changning Road, Shanghai 200050, China

³Helmholtz-Zentrum Dresden-Rossendorf, Institute of Ion Beam Physics and Materials Research, P.O. Box 510119, 01314 Dresden, Germany

(Received 15 August 2014; accepted 29 September 2014; published online 15 October 2014)

Dark current mechanisms of terahertz quantum-well photodetectors (THz QWPs) are systematically investigated experimentally and theoretically by measuring two newly designed structures combined with samples reported previously. In contrast to previous investigations, scattering-assisted tunneling dark current is found to cause significant contributions to total dark current. A criterion is also proposed to determine the major dark current mechanism at different peak response frequencies. We further determine background limited performance (BLIP) temperatures, which decrease both experimentally and theoretically as the electric field increases. This work gives good description of dark current mechanism for QWPs in the THz region and is extended to determine the transition fields and BLIP temperatures with response peaks from 3 to 12 THz. © 2014 AIP Publishing LLC. [<http://dx.doi.org/10.1063/1.4898036>]

I. INTRODUCTION

Presently, terahertz quantum-well photodetectors (THz QWPs) have emerged as one promising candidate to realize compact, high speed, and high frequency detectors for the THz region due to the characteristics of intersubband transitions and unipolar transport properties. Compared with other detectors in THz region, such as Si bolometers, pyroelectric detectors made from LiTaO₃ crystals and heterodyne detectors made from low temperature superconductor films,^{1,2} THz QWPs have their own advantages. The first and foremost important advantage relates to the availability of a mature material and processing technology for QWPs based on GaAs, which makes it possible to fabricate large-scale uniform, high resolution, and long-term stable THz QWP focal plane arrays. Second, they are narrow band and enable wide wavelength coverage by adjusting the intersubband transition energy. The other distinct advantage of THz QWPs is their intrinsic high speed due to the inherent short carrier lifetime, which helps to create new applications in, for example, environmental remote sensing of molecules and long-wavelength laser-based communication.³ THz QWPs are designed as a natural extension of quantum well infrared (IR) photodetectors⁴ and many researchers have been conducted to achieve better performance^{5–7} after their first experimental demonstration.^{8–10} Dark current, which has been investigated extensively in mid-infrared QWPs,⁴ is a key parameter to determine the performance of QWPs. Different from mid-IR QWPs, QWPs in THz region have lower barrier height, lower working temperature, and bias. Additional physical effects including exchange-correlation and depolarization, which could be ignored in mid-IR QWPs

must be included. However, only limited investigations have been carried out on dark current mechanisms of THz QWPs. Recently, Ferré *et al.* exploited many-body effects to improve the design of THz QWPs for lower dark current.¹¹ Tan *et al.* have simulated the dark current of a 3.2 THz QWP and got the conclusion that the thermionic emission mechanism is the major mechanism to dark current.¹² But previous investigations have only been conducted on the basis of one specific sample and detailed dark current mechanisms of THz QWPs have not been elaborated.

In this paper, we systematically investigate the dark current mechanism of THz QWPs ranging from 3 to 12 THz experimentally and theoretically by using newly designed QWP structures (L924, L925) combined with other samples (v265, v266, v267) initially proposed by Liu.⁸ We also propose the transition fields at different peak frequencies for THz QWPs as a criterion to determine the dominant dark current mechanism. Moreover, experimental and theoretical results on background limited performance (BLIP) temperature considering different dark current mechanisms are given and discussed in detail.

II. THEORY AND MODEL

Fig. 1 shows the schematic plot of the physical processes contributing to dark current of THz QWPs. First, interwell tunneling, which could be neglected due to the designed wide barriers, involves electrons scattering from the ground state in one quantum well (QW) into the next. Second, thermionic emission (TE) refers to thermal excitation of electrons from the upper part (with energy greater than the barrier height) of the ground state to the nonconfined continuum on the top of the barrier. Finally, scattering-assisted Fowler-Nordheim tunneling (SAT)

^{a)}Electronic mail: yuehzhang@sjtu.edu.cn.

^{b)}Electronic mail: h.schneider@hzdr.de

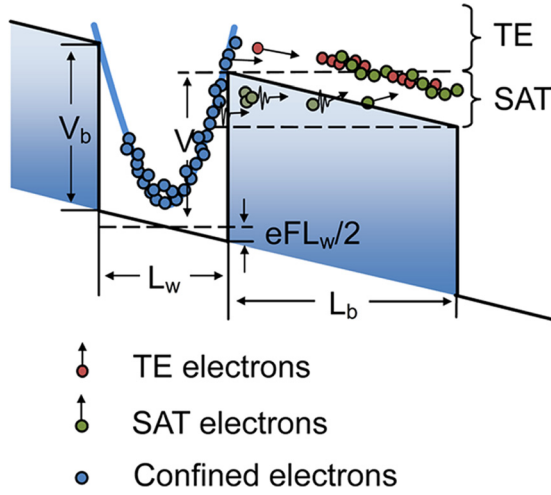


FIG. 1. Schematic plot of physical regimes contributing to the dark current of THz QWPs. Interwell tunneling dark current is neglected due to our designed wide barriers.

means confined electrons of the ground state slightly below the barrier height could be scattered by either phonons or electrons from QWs into the continuum through the tip of the barriers. L_w and L_b are the QW width and barrier width, respectively. F is the electric field applied to the THz QWP samples. V_b is the original barrier height, while $V = V_b - eFL_w/2$ is the barrier height lowering by applied electric field. According to the emission-capture model, we give the dark current by⁴

$$J_{dark} = \frac{ev(F)\tau_c}{\tau_{scatt}} \int_{E_1}^{\infty} \frac{m}{\pi\hbar^2 L_p} T(E, F) \left[1 + \exp\left(\frac{E - E_f}{k_B T}\right) \right]^{-1} dE. \quad (1)$$

The drift velocity is taken of the usual form $v(F) = \mu F / [1 + (\mu F / v_{sat})^2]^{1/2}$. Values of $\mu = 5000 \text{ cm}^2/\text{Vs}$ for the excited-electron mobility and $v_{sat} = 10^7 \text{ cms}^{-1}$ for the saturated velocity were used in calculation. τ_{scatt} is the scattering time of electrons from the ground state into the continuum state and τ_c is the capture time from the continuum back to the ground state. For sample L925 with transition energy $\sim 47 \text{ meV}$, the life time of excited electron τ_c is mainly determined by optical phonon scattering and electron-electron scattering, which is expected to have similar value as in mid-infrared QWPs. However, for L924 whose transition energy (28 meV) is smaller than the LO phonon energy of GaAs (36 meV), electron-electron scattering becomes the dominant mechanism, which is expected to cause a reduced capture probability and, thus, an increased τ_c . In this model, τ_c and τ_{scatt} just enter linearly and not in the exponent (see Eq. (1) and Eqs. (4) and (5) below). As a result, a small deviation in the estimation of τ_c and τ_{scatt} will have weak impact on the results of dark current and BLIP temperature. So, the scattering time is set as $\tau_{scatt} = 5 \text{ ps}$, the values of life time of excited electrons are set as $\tau_c = 8 \text{ ps}$ for sample L925 and $\tau_c = 10 \text{ ps}$ for L924.⁷ L_p is the period length of the multiple quantum-well structure and equals the sum of QW and barrier widths. E_f is the temperature dependent Fermi level in the QWs given by¹³

$$E_f(T) = k_B T \ln \left[\exp \left(\frac{\pi \hbar^2 L_{dope} N_{3Ddope}}{m^* k_B T} \right) - 1 \right], \quad (2)$$

where N_{3Ddope} is the 3D doping density in the center of GaAs QWs and L_{dope} is the doping length. $T(E, F)$ is the transmission coefficient calculated using Wentzel-Kramers-Brillouin (WKB) approximation. For energy higher than the barrier (for $E > V$), $T(E, F) = 1$. Equation (1) could be simplified in pure TE regime and the dark current obtained corresponds to TE dark current as marked in Fig. 1. For energy less than the barrier height, $T(E, F)$ could be given as⁴

$$T(E, F) = \exp \left[-2 \int_0^{z_c} dz \sqrt{2m_b(V - E - eFz)} / \hbar \right], \quad (3)$$

where m_b is the barrier mass, $z_c = (V - E)/eF$ is defined as the classical tunneling point. As shown in Fig. 1, when $V - eFL_b < E < V$, the dark current obtained corresponds to SAT dark current. When $E_1 < E < V - eFL_b$, the dark current obtained corresponds to interwell tunneling dark current, which is far less than TE and SAT dark current in operation temperatures and biases.

III. EXPERIMENT AND DISCUSSION

A. Devices, fabrication, and measuring

We have designed two THz QWP structures, which were grown on semi-insulating GaAs wafers by molecular beam epitaxy. Both samples (samples L924 and L925) consist of a number of GaAs/AlGaAs QWs sandwiched between 400 nm and 800 nm thick n-type contact layers on the top and bottom sides, respectively, with doping density of 10^{17} cm^{-3} in the contact layers. Detailed design parameters are listed in Table I. The well width, Al fraction, and doping density are optimally designed such that only one energy state E_1 is bound in the QW and the excited state E_2 is close to resonance with the bottom of the barrier conduction band. Also, many-body effects including: Hartree potential energy, exchange-correlation potential energy, and depolarization energy have been taken into consideration in the design.^{7,14-16} The barrier width was chosen nearly five times of the well width to suppress the interwell tunneling dark current. Mesa devices with different sizes were fabricated using standard GaAs processing techniques with metal top contacts. For optical characterization, samples were polished to give rise to a 45° facet and packaged into the standard double-pass back side illumination geometry

TABLE I. Structure parameters of THz QWPs. L_w is the well width, L_b is the barrier width, Al_x is the barrier aluminum fraction, N_{3Ddope} is 3D doping concentration in the center of the well. L_{dope} is the doping region width. N is the number of QWs, ν_p is the measured response peak. The GaAs/AlGaAs MQWs are sandwiched between 400 nm top and 800 nm bottom GaAs contact layer doped with Si to 10^{17} cm^{-3} .

| Sample | L_w (nm) | L_b (nm) | Al_x (%) | N_{3Ddope} (cm^{-3}) | L_{dope} (nm) | N | ν_p (THz) |
|--------|------------|------------|------------|-----------------------------------|-----------------|-----|---------------|
| L924 | 12 | 64 | 4 | 1×10^{17} | 7 | 35 | 6.78 |
| L925 | 9.6 | 50 | 7 | 1×10^{17} | 9.6 | 40 | ~ 11.37 |

with an internal incident angle of 45° . All samples' characteristics were performed in a helium cryostat and the photo-current spectra were measured with a Fourier transform infrared spectrometer (Bruker IFS 66 S/V) with glowbar source and a Mylar 6u beam splitter.

B. Dark current mechanisms

Figs. 2(a) and 2(b) show the calculated and measured dark current of samples L924 and L925 at various temperatures. As shown, the calculated dark currents (solid lines), which equal the sum of TE dark current (dotted lines) and SAT dark current (dashed lines), agree well with the experimental measurements (bullets) at different bias voltages and temperatures for both samples. The deviation in the low temperature region (14 K for L924 and 22.5 K for L925) suggests that the measured dark current decreases more slowly than expected below 16 K for L924 and 25 K for L925. This behavior is likely caused by tunneling such as direct interwell and hopping-like via deep-impurity levels in the barrier. The tunneling is much less than TE and SAT at higher temperatures, but makes non-negligible contribution to the dark current in the low temperature region. For sample L924 in Fig. 2(a), SAT dark current is an important part of the dark current at its normal working bias voltages as well as TE dark current. The transition field, defined as the electric field at which SAT dark current equals TE dark current, show an upward trend as 459, 538, 650, 744, 994, and 1298 V/cm with the temperatures of 14, 16, 18, 20, 25, and 30 K, respectively. The reason is that TE dark current increases more quickly than SAT dark current as the temperatures rise, such that bigger transition fields are reached.

In addition, it is interesting to note that the measured dark current becomes larger than the calculated one, when the sample is biased near the breakdown field of 2203 V/cm (0.6 V bias). This breakdown occurs since the extra electrons, which are usually confined in QW can leak across the

barriers due to an efficient ionization of the first QW, as has been discussed in more detail by Gomez *et al.*,¹⁷ Delga *et al.*,¹⁸ and Guo *et al.*¹⁹ However, when it comes to high temperature, most of the confined electrons escape into the continuum already by TE and SAT and the relative contribution by extra leakage due to ionization becomes negligible. For sample L925 shown in Fig. 2(b), the measurement and theoretical calculations are carried out up to 4100 V/cm (1 V bias) and temperatures from 22.5 to 32.5 K. The transition fields are 848, 993, 1143, 1277, and 1440 V/cm for temperatures of 22.5, 25, 27.5, 30, and 32.5 V, which are far below the breakdown field of 4108 V/cm. Moreover, the dark current simulations are also performed for the samples reported in Ref. 8. For sample v267 with peak response frequency of 3.2 THz, we reach the same conclusion as Tan,¹² i.e. that the TE contribution is dominant in dark current. The main reason is that the maximum breakdown field (107 V/cm) that could be applied at the operation temperature is much smaller than the transition fields, such that the SAT regime could never be reached for this sample. For sample v266 with response peak position of 5.4 THz, both TE dark current and SAT dark current are significant parts in its working electric fields and temperatures.

To provide a fundamental criterion to determine which mechanism is dominant in total dark current for THz QWPs with different peak response frequencies, we give the calculated transition fields in Fig. 3. The temperatures used are the BLIP temperatures when TE dark current dominates and the structure parameters used are optimally designed in Ref. 7. As shown, if the THz QWP device is operated at a bias below the transition field, TE process is the major contribution for the dark current. Otherwise, the SAT dark current is dominant. Measured breakdown fields and calculated transition fields for samples v265, v266, v267, L924, and L925 are also presented in Fig. 3. The little difference in structure

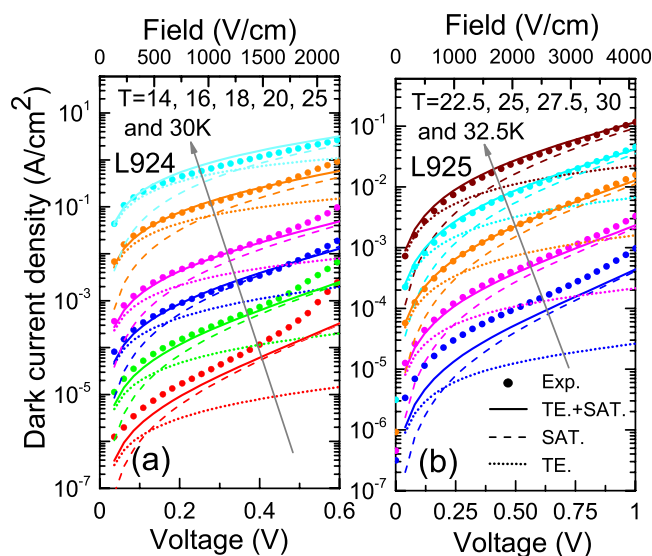


FIG. 2. Experimental (bullets) and calculated (dotted, dashed, and solid lines) dark current of samples (a) L924 and (b) L925 at various temperatures. The dashed and dotted lines represent TE dark current and SAT dark current, respectively. The solid lines are the total dark current.

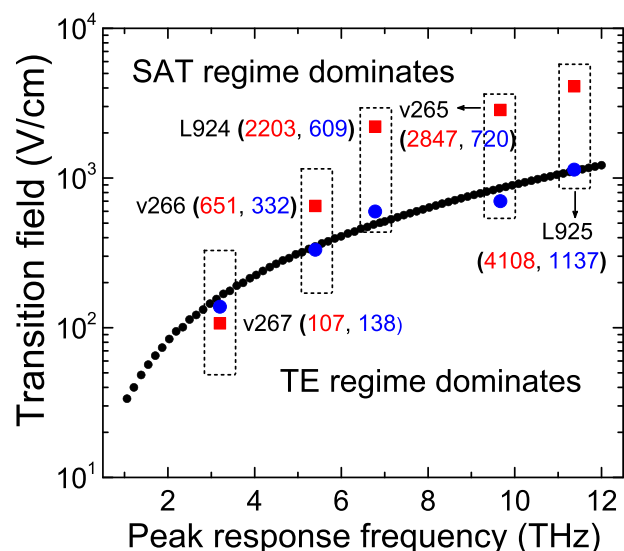


FIG. 3. Calculated transition fields for THz QWPs with different response peak frequencies. Structure parameters used are designed in Ref. 7. Temperatures used are the BLIP temperatures when TE dark current is the dominant. Measured breakdown fields (solid squares) and calculated transition fields (solid circles) are also presented for samples v265, v266, v267, L924, and L925.

parameters of experimental samples and designed ones may account for the small deviation in the transition fields. Except v267, whose dark current mechanism is always TE dominant due to its breakdown field less than transition field, SAT dark current could be the major mechanism for all other samples in normal operation bias. From the breakdown fields and transition fields shown, we can conclude that TE is the major dark current mechanism for THz QWPs with very low peak response frequencies (below about 4 THz) in their working biases, while SAT dark current can be much larger than TE for higher frequency THz QWPs in their normal operation biases. As a summary, the SAT process is a very significant dark current regime for THz QWPs since higher bias leads to increased responsivity, which helps to realize the stable operation of THz QWP devices by reducing the influence of unwanted noise sources (e.g., amplifier noise).

C. BLIP temperature

On the basis of the above systematical investigation on dark current mechanisms of THz QWPs, we further introduce the BLIP temperature taken as the temperature at which background photocurrent equals the dark current, which is a significant parameter reflecting the performance of QWPs. BLIP temperatures were measured by comparing current-voltage (I - V) curves under dark condition (I_d) and under a 300 K background (I_{bg}) with 90° field of view (FOV) at different temperatures. Measured I - V curves are shown in Figs. 4(a) and 4(b) for samples L924 and L925, respectively. As is shown in Fig. 4(a) for L924, when the bias is increased to a threshold value of 0.6 V, the currents show an abrupt increase of more than one order of magnitude, which is due to barrier breakdown caused by ionization of the first QW.¹⁷ For L925 in Fig. 4(b), when temperature dropped below 20 K, the dark currents stop decreasing and remain constant. This behavior is partly due to the remaining tunneling. The tunneling dark current is so low as compared to the background photocurrent that it could be ignored when the device works in BLIP regime. To theoretically investigate the BLIP temperatures, we first give the photocurrent by

$$J_{\text{photon}} = e\phi_{B,ph}\eta g_{\text{photo}}, \quad (4)$$

where $\phi_{B,ph}$ is incident photon flux number given by $\phi_{B,ph} = \int d\nu (\pi \sin^2 \frac{\theta}{2}) \eta(\nu) L_B(\nu)$. $L_B(\nu)$ is the photon irradiance, which can be written as $L_B(\nu) = \frac{2\nu^2}{c^2} \frac{1}{e^{h\nu/k_B T_B} - 1}$, T_B is background temperature. The spectral lineshape $\eta(\nu) = \frac{\Gamma^2}{(h\nu - h\nu_p)^2 + \Gamma^2}$ with the peak response frequency ν_p , the cut-off response frequency $\nu_c = 1.1 \times \nu_p$, and the Lorentzian linewidth constant $\Gamma = h\nu_c - h\nu_p$ matches well with the shapes of measured photocurrent spectra for both samples shown in Fig. 3(c). The main dark region from 256 to 292 cm^{-1} in sample L924 is due to GaAs optical phonon absorption in the substrate, other small features such as the dips at 312 and 338 cm^{-1} are caused by two-phonon absorption. The dip at 362 cm^{-1} in both samples corresponds to the AIAs-like phonon absorption.

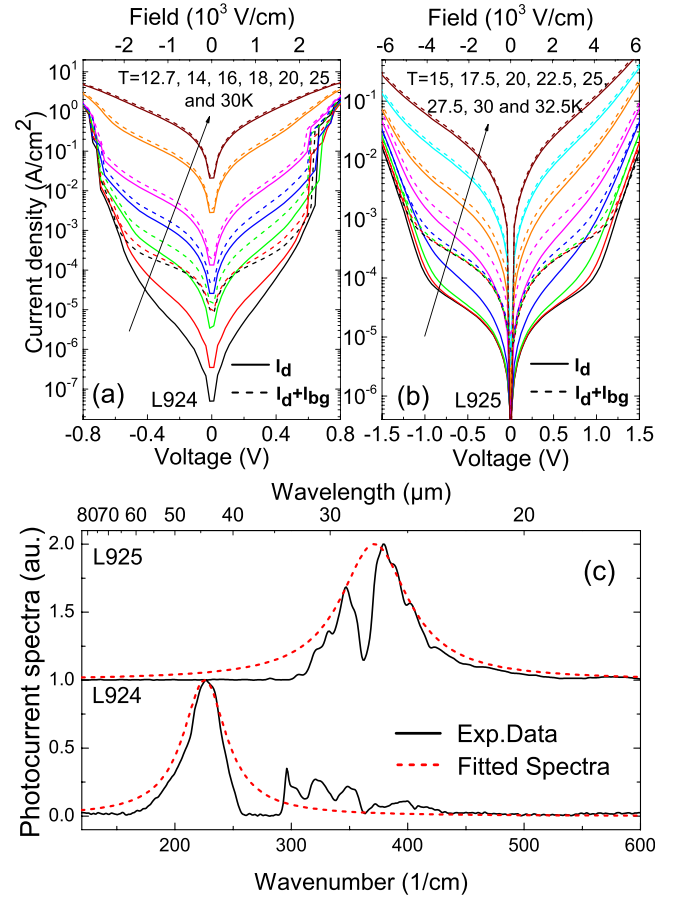


FIG. 4. Current-voltage curves under dark condition (solid lines) and under 90° FOV 300 K background (dashed lines) for samples (a) L924 and (b) L925 at various temperatures. (c) Measured photocurrent spectra (solid lines) and fitted ones (dashed lines) for samples L924 and L925.

The quite broad photoresponse spectra for both samples indicate that the intersubband transitions are of bound-to-continuum type. For this bound-to-continuum case, the escape process of excited electrons takes little time, i.e., once an electron is excited, it is already in the continuum. In this case, an escape probability equal to one is a good approximation for practical proposes and as a result, the photoconductive gain is taken as $g_{\text{photo}} \approx \tau_c \nu / NL_p$. The absorption efficiency is given by $\eta = \frac{e^2 \hbar}{4\epsilon_0 n_r m_w^* c} \frac{\sin^2 \theta}{\cos \theta} N_{3D} D_{\text{dope}} f \frac{1}{\pi} \frac{\Gamma}{(h\nu - E_{21})^2 + \Gamma^2}$, $\theta = 45^\circ$ is the angle between THz radiation propagating direction and QW's growth direction, and $f = \frac{4\pi m_w^* \nu}{\hbar} |\langle \varphi_2 | z | \varphi_1 \rangle|^2$ is the oscillator strength. From Eqs. (1) to (4), the BLIP temperature is determined by the following equation:

$$\phi_{B,ph} \eta^{(1)} \tau_{\text{scatt}} = \frac{m}{\pi \hbar^2} \int_{E_i}^{\infty} T(E, F) \left[1 + \exp\left(\frac{E - E_f}{k_B T}\right) \right]^{-1} dE, \quad (5)$$

where $\eta^{(1)}$ is the absorption efficiency per QW.

In Fig. 5(a), measured BLIP temperatures under different electric fields are shown (symbols) for samples v265, v266, L924, and L925. Calculated BLIP temperatures versus bias voltages are also presented with solid lines, which agree

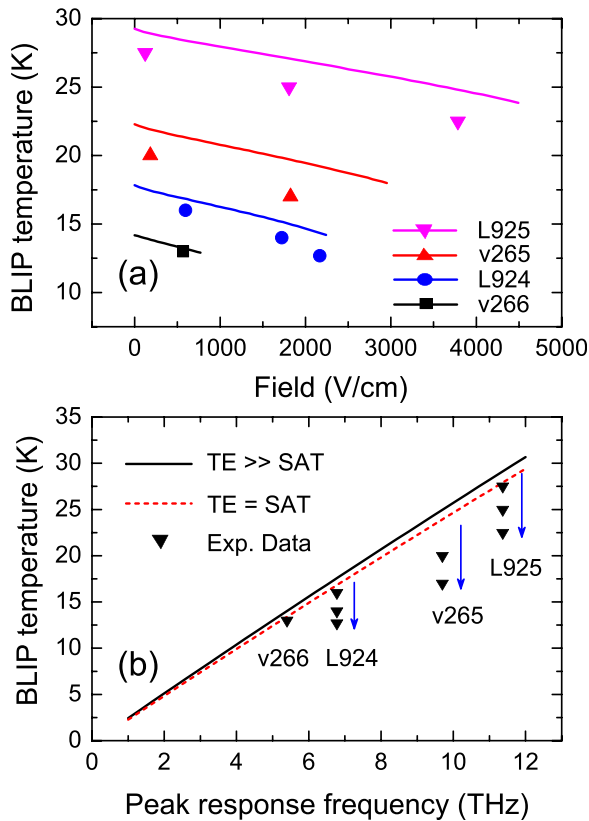


FIG. 5. (a) Measured (symbols) and calculated (solid lines) BLIP temperatures at different fields for samples v266, L924, v265, and L925. In the calculation, the maximum indicated electric fields are the respective breakdown fields. (b) Measured (symbols) BLIP temperatures for samples v266, L924, v265, and L925 at different biases and calculated BLIP temperatures for different peak response frequencies, when sample is operated at a small bias such that TE is the dominant dark current (solid line) and a bias at which TE equals SAT (dashed line). Vertical arrows indicate the field-induced decrease of the BLIP temperature.

reasonably well with the experimental data. As shown, an obvious decrease of BLIP temperatures with increasing electric field is found due to the sharp increase of SAT dark current. For samples L925 and v265, measured BLIP temperatures are lower than the calculated ones. This may partly be caused by the decrease of the photon flux by phonon absorption, which could be seen from the photocurrent spectra in Fig. 4(c). In addition, it is hard to determine the real intersubband transition frequencies of these two samples due to the phonon absorptions, which will also be responsible for the deviation of the calculated BLIP temperature. In particular, it should be noted that for a THz QWP working under a certain bias in BLIP regime, it is usually not appropriate to increase the applied electric field for larger output signals since the signal to noise ratio of the detector will be sacrificed due to the dramatically rising SAT dark current. However, if larger signal is preferred and the increase of the bias is inevitable, the operation temperature of the device should be lowered to reduce the dark current for reaching new BLIP regime.

Fig. 5(b) illustrates the calculated BLIP temperature for THz QWPs with different peak detection frequencies considering the effect of applied electric field on the dark current. As shown, when the sample is operated at small bias, i.e., TE

is the dominant dark current, the calculated BLIP temperature obtained is consistent with calculated and experimental results reported before.^{8,9} When the applied electric field increases towards the transition field such that TE dark current equals the SAT dark current, the BLIP temperatures obtained are slightly lower than BLIP temperatures when TE dominates. When the electric field approaches the breakdown field, SAT is always the major dark current process for QWP samples with higher peak response frequencies in the THz region, which will further decrease the BLIP temperature. Experimental measured BLIP temperatures for samples v266, L924, v265, and L925 are presented and show a decrease trend with bias increasing. In particular, the BLIP temperatures for sample L924 (6.78 THz peak frequency) and L925 (11.37 THz) are about 20% lower at high bias close to the breakdown field (2203 and 4108 V/cm, respectively) than at low bias.

IV. CONCLUSION

In conclusion, we have investigated the dark current mechanism of THz QWPs experimentally and theoretically using two newly designed THz QWPs in combination with existing samples. By comparison of the calculated dark current with experiments, we illustrate that the SAT dark current is a significant part of the total dark current as well as the TE dark current under normal working bias. In the operation of THz QWPs, high working bias is always preferred for increased responsivity, such that SAT dark current will occur and should be taken into account in analysis of THz QWPs' performance. We also proposed the transition fields for THz QWPs with different response peaks as a criterion to determine the main mechanism of dark current. Moreover, considering the sharp increase of SAT dark current with bias voltage, calculated BLIP temperatures show a downward trend, which was confirmed by the experiments. For further description, we give the BLIP temperatures for THz QWPs with different peak response frequencies accounting for the contribution of SAT dark current. Our theoretical and experimental results show that SAT, which is well known for mid-infrared QWPs but has been ignored in previous investigations for QWPs in THz region,^{5,7,12,14,16-18} should be noted to play a key role in total dark current, and its further effect on the performance such as BLIP temperature has to be taken into consideration.

ACKNOWLEDGMENTS

The authors were deeply indebted to Professor H. C. Liu for his huge contribution to this work, until his sudden death in October 2013. The authors also thank E. H. Linfield and L. H. Li for the growths of wafers. This work was supported in part by 863 Program of China (2011AA010205), the Natural Science Foundation of China (91221201, 61234005, and 11074167), and the National Major Basic Research Projects (2011CB925603).

¹M. Hajenius, J. J. A. Baselmans, A. Baryshev, J. R. Gao, T. M. Klapwijk, J. W. Kooi, W. Jellema, and Z. Q. Yang, *J. Appl. Phys.* **100**, 074507 (2006).

- ²P. Khosropanah, W. Zhang, J. N. Hovenier, J. R. Gao, T. M. Klapwijk, M. I. Amanti, G. Scalari, and J. Faist, *J. Appl. Phys.* **104**, 113106 (2008).
- ³X. G. Guo, J. C. Cao, R. Zhang, Z. Y. Tan, and H. C. Liu, *IEEE J. Sel. Top. Quantum Electron.* **19**, 8500508 (2013).
- ⁴H. Schneider and H. C. Liu, *Quantum Well Infrared Photodetectors: Physics and Applications* (Springer, 2007).
- ⁵H. C. Liu, H. Luo, C. Y. Song, Z. R. Wasilewski, A. J. S. Thorpe, and J. C. Cao, *Infrared Phys. Technol.* **50**, 191 (2007).
- ⁶H. Schneider, H. C. Liu, S. Winnerl, C. Y. Song, M. Walther, and M. Helm, *Opt. Express* **17**, 12279 (2009).
- ⁷S. Zhang, T. M. Wang, M. R. Hao, Y. Yang, Y. H. Zhang, W. Z. Shen, and H. C. Liu, *J. Appl. Phys.* **114**, 194507 (2013).
- ⁸H. Luo, H. C. Liu, C. Y. Song, and Z. R. Wasilewski, *Appl. Phys. Lett.* **86**, 231103 (2005).
- ⁹H. C. Liu, C. Y. Song, A. J. S. Thorpe, and J. C. Cao, *Appl. Phys. Lett.* **84**, 4068 (2004).
- ¹⁰M. Graf, G. Scalari, D. Hofstetter, J. Faist, H. Beere, E. Linfield, D. Ritchie, and G. Davies, *Appl. Phys. Lett.* **84**, 475 (2004).
- ¹¹S. Ferré, S. G. Razavipour, and D. Ban, *Appl. Phys. Lett.* **103**, 081105 (2013).
- ¹²Z. Y. Tan, X. G. Guo, J. C. Cao, H. Li, X. Wang, S. L. Feng, Z. R. Wasilewski, and H. C. Liu, *Semicond. Sci. Technol.* **24**, 115014 (2009).
- ¹³B. F. Levine, *J. Appl. Phys.* **74**, R1 (1993).
- ¹⁴M. Graf, E. Dupont, H. Luo, S. Haffouz, Z. R. Wasilewski, A. J. S. Thorpe, D. Ban, and H. C. Liu, *Infrared Phys. Technol.* **52**, 289 (2009).
- ¹⁵X. G. Guo, Z. Y. Tan, J. C. Cao, and H. C. Liu, *Appl. Phys. Lett.* **94**, 201101 (2009).
- ¹⁶X. G. Guo, R. Zhang, H. C. Liu, A. J. S. Thorpe, and J. C. Cao, *Appl. Phys. Lett.* **97**, 021114 (2010).
- ¹⁷A. Gomez, V. Berger, N. Pere-Laperne, and L.-A. de Vaulchier, *Appl. Phys. Lett.* **92**, 202110 (2008).
- ¹⁸A. Delga, L. Doyennette, A. Buffaz, V. Berger, F. R. Jasnot, L. A. de Vaulchier, N. Péré-Laperne, and H. C. Liu, *J. Appl. Phys.* **110**, 013714 (2011).
- ¹⁹X. G. Guo, L. L. Gu, M. Dong, J. C. Cao, H. C. Liu, and F. M. Guo, *J. Appl. Phys.* **113**, 203109 (2013).